BNL-227638-2025-JAAM

Design of the EIC hadron storage ring stripline injection kicker with a novel impedance tuning capability

M. P. Sangroula

To be published in "Physical Review Accelerators and Beams"

February 2025

Collider Accelerator Department

Brookhaven National Laboratory

U.S. Department of Energy

USDOE Office of Science (SC), Nuclear Physics (NP)

DISCLAIMER

Design of the EIC hadron storage ring stripline injection kicker with a novel impedance tuning capability

M. P. Sangroula,* C. J. Liaw, C. Liu, J. Sandberg, N. Tsoupas, and B. Xiao
Collider Accelerator Department, Brookhaven National Laboratory, Upton, New York 11973, USA

X. Sun
Argonne National Laboratory, Advanced Photon Source, Argonne, Illinois 60439, USA

(Received 26 August 2024; accepted 24 January 2025; published 18 February 2025)

The Electron-Ion Collider (EIC), to be built at Brookhaven National Laboratory, will be a high luminosity ($\sim 10^{34}$ cm^{-2} s^{-1}) nuclear science facility. To facilitate EIC experiments, the existing yellow ring of the Relativistic Heavy Ion Collider (RHIC) will be reconfigured to serve as the Hadron Storage Ring (HSR). Designing a stripline injection kicker for the HSR beams, with high magnetic rigidity (~82 Tm), poses some technical challenges due to the required large pulsed voltage with long flattop duration, very fast rise time, expected shorter bunch spacing, and potential heating due to higher peak current. In addition, minimizing impedance mismatch in the transition region between the feedthrough and the stripline electrode is challenging. This paper focuses on the mechanical design and optimization of the HSR injection kicker, highlighting a novel impedance tuning capability achieved through an innovative kicker aperture adjustment mechanism. We comprehensively cover the design, including impedance optimization (both beam coupling and characteristic), beam-induced heating, and thermal analysis, and investigation of the maximum electric field due to high voltage signal excitation to ensure safe and reliable operation.

DOI: 10.1103/PhysRevAccelBeams.28.020401

I. INTRODUCTION

The Electron-Ion Collider (EIC) [1,2] is being built to provide collisions between polarized beams of electrons and ions at center-of-mass energies ranging from 20 to 140 GeV/nucleon. The primary goal of constructing such an advanced accelerator is to address fundamental physics questions within nucleons, unraveling mysteries related to mass and spin origins.

Figure 1 presents a schematic view of the EIC layout, featuring counterpropagating beams of electrons and ions colliding at the primary detector. While there is a plan to install a second detector, the baseline design does not include this feature. The EIC modifies one of the two Relativistic Heavy Ion Collider (RHIC) rings, referred to as the "yellow" ring [3], by including the insertion of a race-track-shaped copper-coated stainless steel beam screen with a cooling channel to accommodate a shorter hadron beam. The well-established hadron beam parameters in the current RHIC facility align closely with EIC Hadron Storage Ring (HSR) requirements, except for the total hadron beam current, which will triple due to increased bunch numbers and decreased bunch length. EIC will have a new Electron Storage Ring to provide polarized electron beams up to 18 GeV for collisions with polarized protons or heavy ions.

One of the challenging tasks for the EIC is to design a hadron beam injection system that efficiently injects various beams from the Alternating Gradient Synchrotron (AGS) into the HSR. We plan to use the stripline injection system for this. The design of a stripline injection kicker for the HSR faces several technical challenges, including the need for high pulsed voltage with a long flattop duration, very fast rise time, high surface electric field due to large voltage, expected shorter bunch spacing, and potential heating due to high peak current [5]. In addition, minimizing impedance mismatch in the transition region between the feedthroughs and stripline electrodes poses another challenging effort.

Table I compares the stripline kicker parameters at different accelerator facilities. The comparison shows that the EIC HSR has the most rigid beam which demands a large number of kicker modules even for a small deflection. The expressions for a deflection angle and detailed calculation for the number of kickers are discussed in Sec. II. Additionally, achieving a longer flattop with high voltage and very fast rise time is a challenging job. Advanced Light Source Upgrade (ALS-U) [6], reported a flattop of 50 ns, but the corresponding required voltage is ±5.4 kV only.

*Contact author: msangroul@bnl.gov

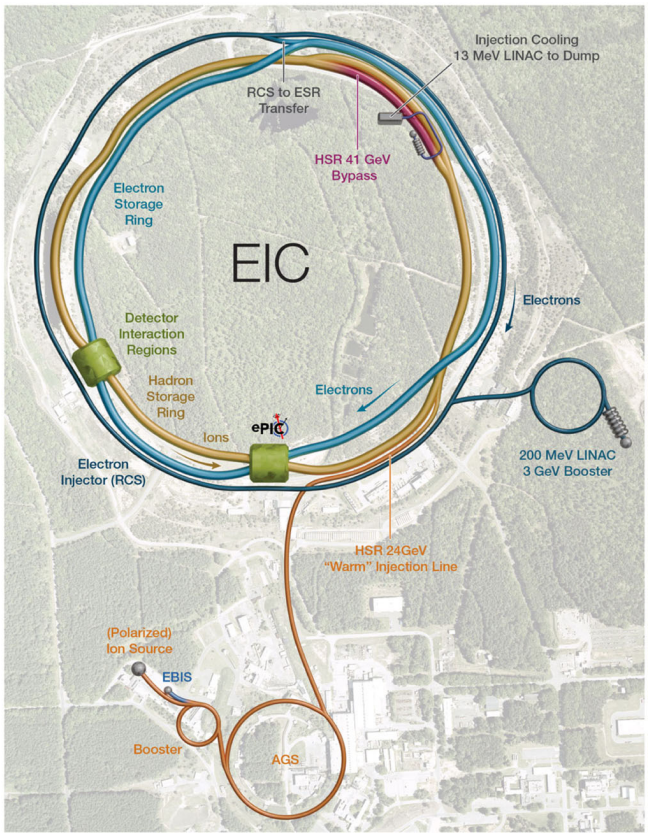

FIG. 1. Schematic layout of the EIC complex [4]. Electrons and ions counterpropagate, respectively, in the blue and yellow rings.

Thus, designing an HSR stripline kicker that requires high voltage along with a long flattop is a real challenge.

This paper is organized as follows: In Sec. II, we introduce basic concepts for the stripline kicker providing brief mathematical expressions based on those found in Refs. [5,7,8] and describe the two modes of operation associated with it. Section III outlines the preparation of the 2D and 3D geometry along with the resolution of the observed discrepancy in the characteristic impedance value between two electromagnetic codes. In Sec. IV, we report on our novel kicker design concept, which incorporates an impedance tuning capability, including some design updates. Section V details the optimization techniques we employed to minimize the beam coupling impedance and to match the characteristic impedance. Section VI presents the beam-induced heating and thermal analysis for this kicker. Finally, in Sec. VII, we discuss the maximum electric field simulation to ensure its safe and reliable operation.

II. STRIPLINE KICKER

A stripline kicker, also called an electromagnetic kicker, consists of two parallel electrodes (striplines). A cartoon image of the stripline kicker is shown in Fig. 2. Each electrode forms a transmission line with the adjacent grounded beam pipe for an external transverse electromagnetic (TEM) mode [5,8]. This device employs both electric and magnetic forces to impart a kick to the incoming beam. The external pulser (amplifier) must excite a TEM mode traveling in the opposite direction to the beam so that the electric and magnetic forces on the beam add rather than cancel. Each end of the two parallel electrodes connects to a coaxial feedthrough. We apply pulsed voltages of equal amplitude but opposite polarity via downstream feedthroughs to generate mostly a uniform electromagnetic field between the electrodes.

Basic analytical expressions on a stripline kicker can be found in articles [5,8–10]. When a charged particle q with energy E traverses stripline electrodes of length L, it experiences a deflection angle,

$$\Delta\theta = 2g_{\perp}\left(\frac{qV}{E}\right)\frac{L}{d}, \tag{1}$$

relative to its reference or initial orbit. Here, $g_{\perp}$ is the transverse geometry factor given by

$$g_{\perp} = \tanh\left(\frac{\pi w}{2d}\right), \tag{2}$$

V is the pulse voltage amplitude, d is the gap between the parallel electrodes, and w is the width of the stripline. Although the analytical expression of $g_{\perp}$ is for striplines with flat electrodes, it still provides a good estimate for

TABLE I. Review of the stripline injection/extraction kicker parameters at different facilities.

Facility	Beam species	Beam rigidity (Tm)	Rise time (ns)	Voltage (kV)	Bunch length (ns)	Electrode length (mm)	Flat top (ns)	Total deflection (mrad)
EIC HSR	Proton	~82	~7	±16.0	25	900	>31	0.77
APS-U	Electron	~20	~2	±15	0.08–0.1	710	~7	3.27
ALS-U	Electron	~6.67	<10	±5.4	0.12–0.2	500	50	3.5
CLIC PDR	Electron	9.54	428/1000	±17.0	3.2/4.6	1639	900/160	…
HEPS	Electron	~20	…	±16.9	…	300	1.611	…
ILC DR	Electron (positron)	16.67	<3–9	±5	…	300	…	0.6
DAΦNE	Electron (positron)	0.3	<6	±25	35 mm	850	5.0	…

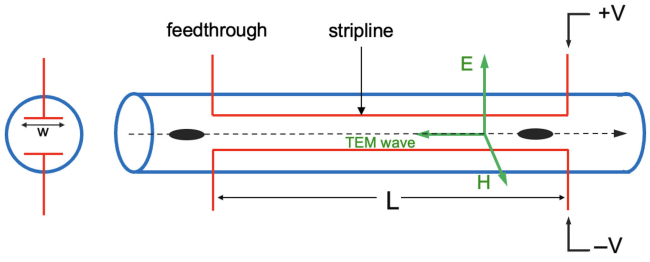

FIG. 2. A cartoon image of the stripline kicker. The cross section with flat electrodes of width w (left) and a side view showing the TEM wave counterpropagating to the beam direction (right).

systems with curved electrodes. Generally, the value of $g_\perp$ is close to unity. In our case, its value is ∼0.94.

We can express Eq. (1) in terms of beam rigidity $B\rho$, where ρ is the radius of the beam orbit in a dipole field B, using the relation [10,11]

$$B\rho\,[\mathrm{Tm}] = 3.3356\,E\,[\mathrm{GeV}]. \tag{3}$$

For example, the EIC proton beam with a beam energy of 24.58 GeV provides the beam rigidity of ∼82 Tm. Thus, a kicker with $L = 0.9$ m, $a = 59$ mm, and $w = 66.2$ mm produces a deflection angle of 3.74×10^{-5} radians with an applied voltage of $V = \pm 16.0$ kV, using Eq. (1). We need about 20 kickers to produce a total deflection of 0.77 mrad (assuming the beam displacement at the septum location is 5.4 cm). The number of kickers can be reduced if the required pulsed voltage is increased. The design parameters for the HSR injection kicker are found in Table II [5,12].

The length of a stripline depends on the different parameters. Since the external pulse counterpropagates into the beam direction, the minimum time (t_{min}) at which the kicker has to be turned on to deflect the incoming bunch is given by

$$t_{\mathrm{min}} \geq \tau_r + 2L/c + \tau_f + \tau_b, \tag{4}$$

where τ_r, τ_f, τ_b, and L are, respectively, kicker's rise time and fall time, full bunch length, and length of stripline electrode. Here, we assume the TEM mode propagates with the speed of light c in a vacuum.

For the EIC, hadron bunches from the Alternating Gradient Synchroton (AGS) will be injected on axis into HSR one at a time. Therefore, the rise time needs to be short enough to fit in the gap between two adjacent bunches. The fall time shall not exceed the length of the abort gap which is ∼1 μs, hence it becomes irrelevant. Thus, the length of a stripline kicker, assuming $t_{\mathrm{min}} = \tau_g$ (the gap between two consecutive bunches), is given by

$$L \leq \frac{c}{2}(\tau_g - \tau_r - \tau_b). \tag{5}$$

We selected the maximum electrical length (3 ns = ∼0.9 m) for the stripline with the upper limit for $\tau_r = 9.5$ ns, and with the values of τ_g and τ_b stated in Table II for the EIC proton beam with 1160 bunch patterns. The input pulse having $\tau_r = 7$ ns is chosen in the design specification though its upper limit was 9.5 ns, to leave enough tolerance for variations. Thus, by knowing beam properties along with the pulser characteristics, we determine the length of an injection kicker.

Each stripline electrode with its adjacent ground planes (beam pipe walls) forms a transmission line for TEM waves. Consequently, the stripline kicker functions as two coupled transmission lines, exhibiting two modes: odd mode and even mode. To kick the incoming beam, we operate the stripline kicker in the odd mode. The even mode is excited by the beam when the kicker is off. The detailed theoretical expressions and the schematic of these modes can be found in [13].

When the electrodes are excited with an equal magnitude but opposite polarity voltages (i.e., when the kicker is on), the current flow is in opposite directions in each stripline electrode, creating a virtual on-axis ground plane. This results in an almost uniform electric field between electrodes and the corresponding state is referred to as the odd mode. The odd mode forms two capacitances: C_1 between an electrode and the beam pipe wall, and C_2 between the two electrodes. According to the theory of transmission lines, the characteristic impedance [14,15] of this odd mode is

$$Z_{\mathrm{odd}} = \frac{1}{c\,(C_1 + C_2)}. \tag{6}$$

In contrast, if we excite pulsed signals of the same polarity (kicker is off), the current flows in the same direction on both electrodes creating mostly zero electric fields at the axis and is called even mode (common mode). In other words, when an unkicked beam passes through the kicker, it induces image currents that flow in the same direction in both electrodes. In the even mode, only the capacitance between the electrode and the beam pipe wall, C_1 exists. The characteristic impedance of the even mode is

TABLE II. HSR injection kicker design parameters.

Parameters	Value	Unit
Beam rigidity	∼82	T m
Full bunch length (τ_b)	25	ns
Bunch spacing (τ_g)	40.5	ns
Rise time (τ_r)	7	ns
Voltage per plate	±16	kV
Total deflection angle (θ)	0.77	mrad
Electrode length (L)	0.9	m
Number of kicker units (max)	20	NA

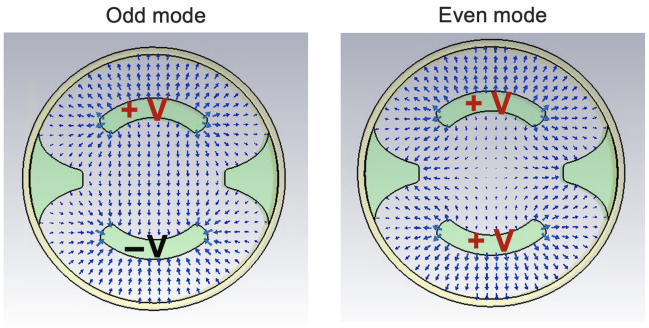

FIG. 3. Simulated electric field patterns at the typical cross section of a stripline kicker for two different modes of operations: odd mode (left) and even mode (right). The striplines (electrodes) are excited with the opposite polarity voltage for the odd mode but, with the same polarity for the even mode.

$$Z_{\text{even}} = \frac{1}{c\,C_1}. \tag{7}$$

The simulated electric field patterns observed at the cross section of the HSR kicker geometry for these two different modes of operations are shown in Fig. 3. The design optimization of a stripline kicker primarily focuses on the odd mode as it is operated in this particular mode.

III. DESIGN OF THE KICKER GEOMETRY

The primary design objectives for the HSR injection kicker are to produce excellent field uniformity between the electrodes and ensure good transmission of input power which is achieved by maintaining the uniform characteristic impedance along its length. In addition, we want a kicker with a low beam coupling impedance [16–18] to reduce the contribution to the overall impedance budget and to enhance beam stability. Finally, we must minimize the value of the maximum electric field to prevent electrical breakdown (or arcing) due to high voltage and to improve power supply reliability. This is obtained by chamfering the sharp edges inside the kicker and optimizing the feedthrough contact geometry.

Before preparing the 2D and 3D kicker geometry, we benchmarked the value of characteristic impedance between two commercial codes for a given geometry.

A. Benchmarking between two codes

We initially used the code OPERA 2D [19] to prepare the initial cross section of the HSR kicker that produces 50 Ω characteristic impedance. Later, we cross-checked this value provided by the code OPERA2D with another 3D electromagnetic code CST [20]. Surprisingly, the same cross section that produced 50 Ω impedance in OPERA 2D resulted in only 47 Ω in CST. Later, we found that the discrepancy in the impedance value is due to the missing of the skin depth effect while using the dc mode of OPERA 2D. Subsequently, we performed simulations using the ac mode of OPERA 2D, which included the skin depth effect. In this case, the characteristic impedance value decreases with frequency and saturates after 1 MHz (similar to Fig. 4). This leads to a good agreement between the two codes, particularly since our kicker operates well above 1 MHz. Then, we increased the diameter of the kicker housing to achieve the desired 50 Ω impedance from the initial value of 47 Ω for the odd mode, as shown in Fig. 4. The details of the 2D cross-section design are discussed in the following subsection.

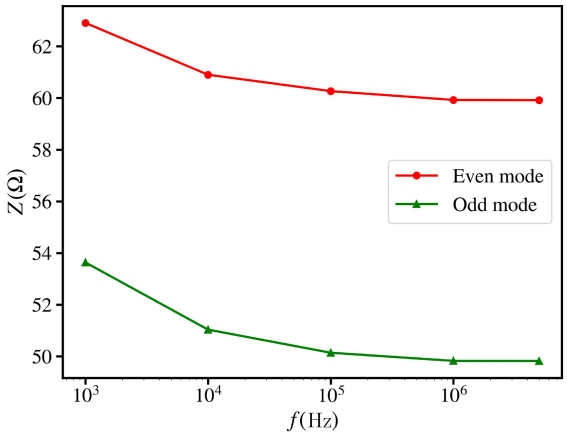

FIG. 4. Variation of the characteristic impedance with frequency using the ac mode of OPERA 2D.

B. 2D cross-section design

The first essential requirement for the 2D cross-section geometry is to produce a characteristic impedance of 50 Ω for the odd mode. This ensures the compatibility with the characteristic impedance of the feedthroughs and the connecting cables. Simultaneously, the second requirement involves maintaining the even mode impedance close to 50 Ω to reduce the beam coupling impedance and beam-induced heating. Unfortunately, we cannot maintain the same 50 Ω impedance for both modes as mentioned in Eqs. (6) and (7). Another initial design constraint was to keep the gap between the electrodes of ∼50 mm due to a slightly higher value of β function in the injection region.

To prepare the initial 2D geometry meeting the specified constraints, we developed two cross sections as shown in Fig. 5(a). The first one had curved electrodes while the other had flat electrodes. Fenders (intrusions) are placed in the cross section, perpendicular to the electrodes, to reduce the deviation between the characteristic impedance of the odd and even modes [6,21].

We compared the electric fields produced by these two geometries to select the appropriate cross section. Figure 5(b) shows the comparison of the electric fields with the gap between electrodes, where solid curves indicate better field uniformity for the cross section with curved electrodes in the central region (region of interest).

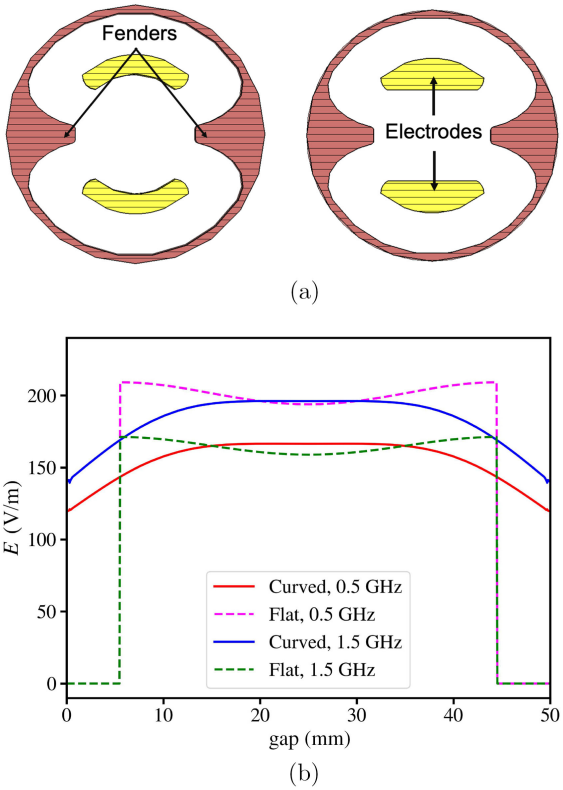

FIG. 5. (a) CAD models showing the kicker cross section with curved electrodes (left) and flat electrodes (right). (b) Electric field comparison between them, where the solid and dashed curves represent curved and flat electrodes, respectively.

Thus, we adopted the curved electrodes for our design. The electric fields were obtained by exciting a Gaussian pulse in CST, within the frequency range of 0–2 GHz through the waveguide port, with a default amplitude of ∼7 V.

The electric field with flat electrodes starts only after a few mm in Fig. 5(b) as the gap between them is slightly lower (∼40 mm) in comparison to curved electrodes. Although the cross section with flat electrodes slightly lowers the characteristic impedance of the kicker by ∼1 Ω, this does not significantly affect the distribution of electric fields. The APS-U kicker design [21] reported better field uniformity for flat electrodes, possibly due to a very narrow spacing <10 mm between them. However, in our case, both CST and OPERA 2D codes demonstrated a more uniform field for the cross section with curved electrodes. A multibunch feedback kicker design for SPEAR 3 also used curved electrodes [22].

After finalizing the kicker's 2D design, we added its essential components to convert it into the 3D design, which we discuss in the following subsection.

C. 3D design

We transformed the 2D kicker geometry into a 3D design, Fig. 6(a), by adding essential components such as feedthroughs (initially ideal coaxial), four venting ports,

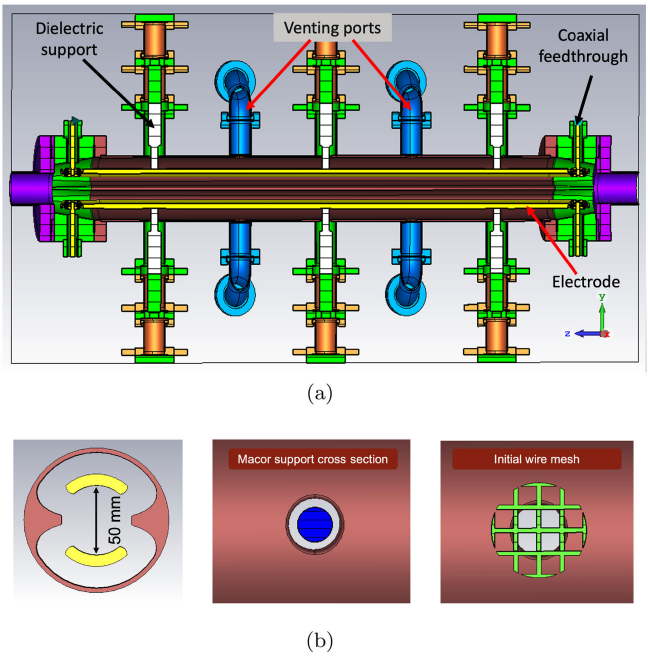

FIG. 6. (a) Initial 3D design of the HSR kicker (top view). (b) Kicker's cross section (left), side view showing the round clearance between the Macor dielectric (blue disc) and kicker housing (middle), and the initial wire mesh (right).

and six dielectric (Macor) supports. Feedthroughs are crucial to excite the kicker by feeding the pulsed power signal. The excitation should originate from the downstream feedthrough, propagate along the stripline electrodes, and finally be absorbed at the upstream feedthrough (50 Ω load).

Venting ports connect vacuum pumps to maintain an ultrahigh vacuum (∼nTorr) inside the geometry. Dielectric (Macor) supports are placed on each stripline electrode to minimize deflection due to the stripline's own weight. To reduce expansion stress due to potential beam-induced heating, the dielectric supports are made slidable along the length of the stripline. These supports help to maintain the stripline's alignment during feedthrough replacement. Adjustable shims are also incorporated on these supports to allow fine-tuning the stripline position, which we discuss in detail in Sec. IV. In addition, there are openings in the kicker housing to accommodate dielectric supports and venting ports. To minimize electromagnetic field leakage via these openings, we maintained a smaller round clearance around the dielectric material, Fig. 6(b) (middle) and placed stainless steel wire mesh (mesh size ∼6.85 mm) on the housing outer surface inside the venting ports, Fig. 6(b) (right).

The HSR kicker deflects the beam in the horizontal plane, and hence the electrodes, feedthroughs, dielectric supports, and venting ports reside on the left and right sides of its housing. Most images shown in this paper are rotated by 90° along the beam axis for the better display of the geometry.

IV. DESIGN UPDATE WITH THE IMPEDANCE TUNING CAPABILITY

Impedance mismatches between the kicker and its connecting components introduce amplitude fluctuations of the pulsed voltage due to multiple power reflections between feedthroughs. This ultimately causes the beam emittance dilution. The pulser for the HSR kicker should generate a flattop of >31 ns. To produce a nearly constant amplitude high kicking voltage along the entire length of a stripline, it is essential to minimize the characteristic impedance mismatch.

The impedance of commercial 50 Ω cables and feedthroughs can vary in the range of 48–52 Ω. Considering this variability, we incorporated a novel *impedance tuning capability* in the kicker design. This key feature ensures proper matching of the kicker's characteristic impedance with connecting components like feedthroughs and coaxial cables [23]. Impedance tuning of the kicker geometry is achieved by adjusting the gap between the electrodes, a process facilitated by adding or removing shims on the dielectric support after the kicker is constructed. The impedance tuning is a part of the assembly process before the installation of the kicker in the beam line. To our knowledge, we are among the first facility to incorporate this impedance tuning mechanism into the stripline kicker design.

To tune the kicker impedance in the range of 48–52 Ω, we further modified its cross section at a minimal design gap of 50 mm between the electrodes. The characteristic impedance of 52 Ω is obtained by increasing the kicker housing diameter from ∼102 to 106 mm, Fig. 7(a). The desired minimum impedance of 48 Ω is accomplished by increasing the gap between the electrodes to ∼62 mm, at a housing diameter of 106 mm. Figure 7(b) depicts the variation of this impedance with the electrode gap which shows that each stripline electrode is tuned up to 6 mm to achieve the desired impedance range between 48 and 52 Ω. We chose the kicker geometry having a standard 50 Ω characteristic impedance with a 59 mm gap between the electrodes for the design optimization.

In addition to incorporating the impedance tuning technique, we updated other design aspects, including the number of dielectric supports, dielectric materials, and the transition geometry between feedthrough and electrodes. Stress analysis using ANSYS [24] for electrode deformation showed that eliminating the midsupport has a negligible impact on preventing the deformation of the stripline electrodes. However, keeping it introduces design complexity with characteristic impedance mismatch. Therefore, we removed the central dielectric support. Initially, we planned to use Macor as a dielectric, which is replaced with alumina due to its robustness in brazing with metals. Additionally, we reduced the length and width of the dielectric material. Finally, we optimized the transition region between the feedthrough and the stripline electrode to reduce the observed impedance mismatch. All these optimizations are discussed in detail in the following section.

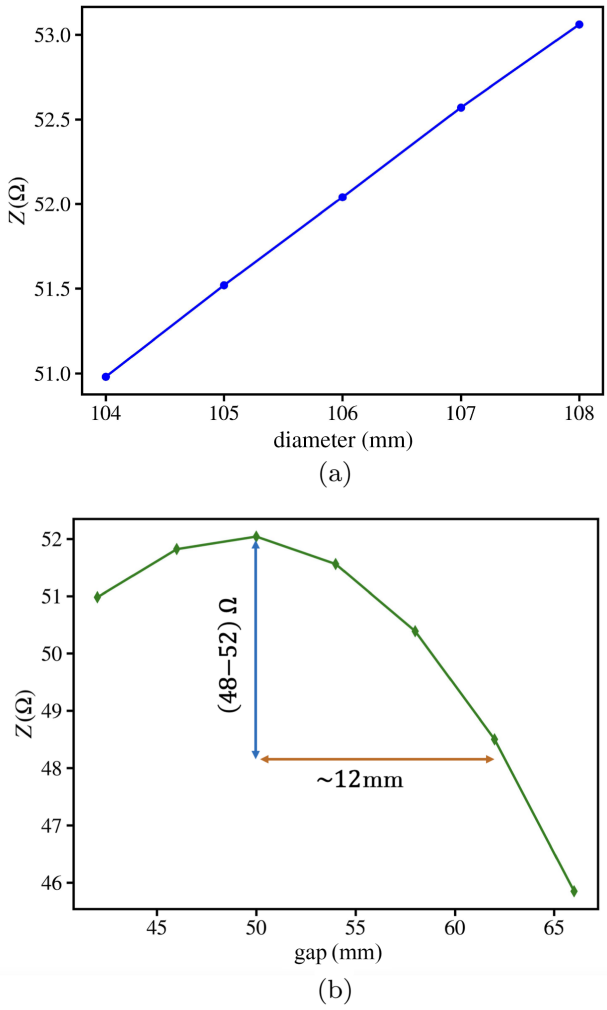

FIG. 7. The variation of the odd mode impedance with the (a) kicker housing diameter and (b) the gap between the electrodes.

V. KICKER GEOMETRY OPTIMIZATION

We optimized the kicker design using CST simulations. The primary objectives are to reduce the beam coupling impedance and match the characteristic impedance.

A. Beam coupling impedance

We used the CST wakefield solver with the beam parameters stated in Table III (including a very short bunch length) to optimize the beam coupling impedance for the injection kicker. At the injection, the bunch length will be longer, and hence the impedance will be lower. Also, the optimization for the coupling impedance is performed for the initial geometry having the electrode gap of 50 mm, and the housing diameter of ∼102 mm. The updated design has a electrode gap of 59 mm and a housing diameter of 106 mm. Since the longitudinal beam coupling impedance scales inversely with the beam pipe radius [16,17], the coupling impedance will be lower in the updated design. The various design optimizations for minimizing the beam

TABLE III. HSR proton beam parameters at store.

Parameters	Value	Unit
rms bunch length (σ_{rms})	60	mm
Average beam curent	0.69	A
Charge per bunch (Q_b)	30.5	nC
Number of bunches (M)	290	NA

coupling impedance are discussed in detail in the following section.

1. Optimization of the end-flange design

The initial end-flange design featured deep pocketlike structures to longitudinally accommodate the ends of the electrode, refer to Fig. 8(a) (left) inside the dark circle. CST simulation for this initial design exhibited wakefield oscillations, the red curve in Fig. 8(b). To identify the component causing the wakefield oscillations, we analyzed the plots for the instantaneous resistive wall (RW) loss due to the kicker's individual components. The RW loss corresponding to the end flange showed fluctuations with time, suggesting that the deep pockets inside the end flange are causing the wakefield oscillations.

To confirm this, we optimized the end-flange geometry by replacing the initial design with a flat flange without any pockets, Fig. 8(a) (right), and reran CST simulations. Figures 8(b) and 8(c), respectively, compare the wakefield and impedance (magnitude) between the initial and the optimized flange designs, where the red curve indicates the original design and the blue curve indicates the optimized design. The wakefield comparison demonstrates that the optimized end-flange design significantly reduces the amplitude of the previously observed wakefield oscillations. Similarly, the resonance peak previously observed at 1.25 GHz in the impedance plothas disappeared.

We slightly shortened the length of the electrodes while optimizing the end-flange design. However, this adjustment did not affect the kicker's performance, as the distance between the two feedthroughs remains the same.

2. Removal of protruded spring contacts

The second component we optimized to reduce the beam coupling impedance is the rf-spring contact geometry at the transition region between the feedthrough's central pin (conductor) and stripline electrode.

The initial design had rf-springs on both sides of the stripline electrode to ensure good rf-contact. However, this design resulted in a protruded contact geometry at the inner surface of the electrodes as shown in Fig. 9(a) (left). Following the optimization of the end-flange design, we performed simulations for the modified geometry containing flat end flange and blended electrodes without sharp edges. Again, we observed small wakefield oscillations, as indicated by the red curve in Fig. 9(b). Analyzing

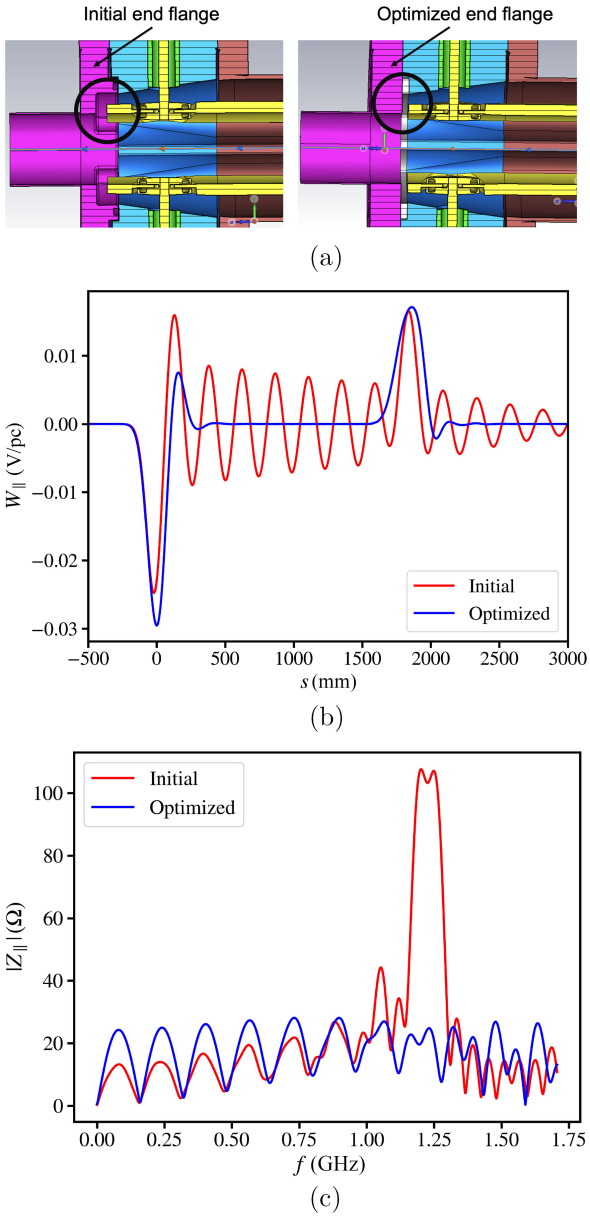

FIG. 8. (a) CAD models showing the end-flange designs. Initial design containing deep pockets (left) and an optimized design without deep pockets (right). Comparison of the (b) wakefield and (c) impedance between these two designs.

the data for the beam-induced RW loss, we found that the protruded contacts caused these oscillations.

To validate, we simplified the contact geometry by removing the protruded springs as shown in Fig. 9(a) (right) and compared the wakefield between the initial and the simplified designs. Figure 9(b) shows this comparison, where the red curve represents protruded contact and the black curve represents the simplified contact. Comparison shows no wakefield oscillation for the simplified geometry. Therefore, we optimized the contact region by removing these protruded contacts along with the incorporation of tapered electrodes (will discuss later) as shown in Fig. 10.

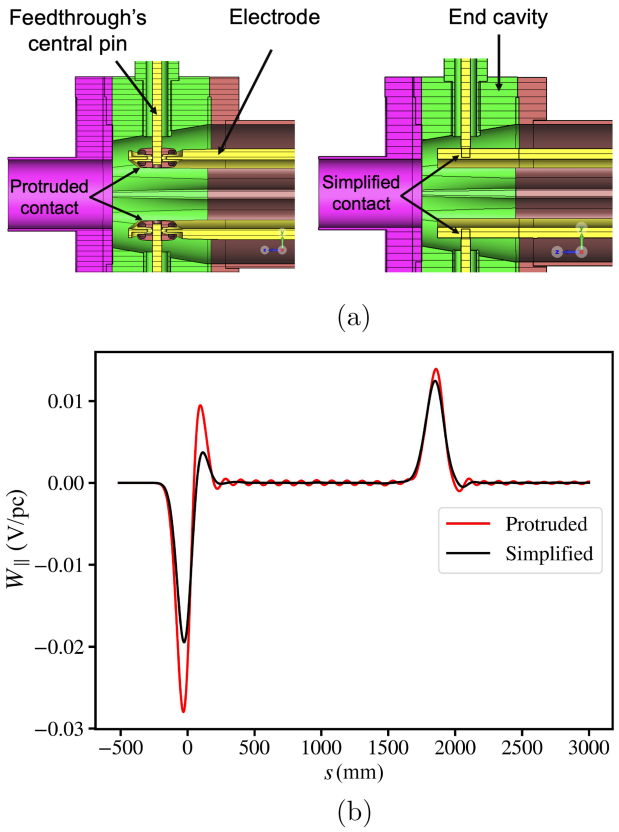

FIG. 9. (a) CAD model of the contact geometry with a protruded spring contact (left) and a simplified contact (right) in the end flange. (b) Wakefield comparison between these two geometries.

3. Clearance aperture around dielectric

The optimization of the end-flange design and protruded spring contact was conducted without including the kicker's essential components, namely dielectric supports and venting ports to save computational resources. After optimizing these two components, we included the dielectric supports. The inclusion of these supports in CST simulations again introduced small wakefield oscillations, caused by the large circular aperture around the dielectric material. To eliminate the observed wakefield oscillations, we reduced the radial dimension of the hole from the initial ∼6 to ∼4 mm.

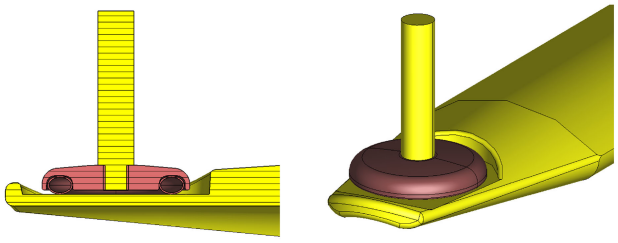

FIG. 10. CAD model of the optimized contact geometry with tapered electrode in a cut view (left), and a perspective view (right).

Finally, we included venting ports that initially had wire mesh inside [Fig. 6(b), right]. We replaced the mesh with a disc containing small holes (Fig. 11) to avoid any field leakage. Since the dimension of these holes is relatively small (2.39 mm), no wakefield oscillations are observed.

Thus, we continuously optimized the beam coupling impedance to achieve consistent results both with and without essential kicker components, including venting ports and dielectric supports.

4. Optimization of the end cavity

Finally, we investigated the possibility of optimizing the end-cavity design by lowering the value of the wake-loss factor, as mentioned in a recent paper on the injection kicker design [25]. For this, we changed the tapering strength (the intensity of taper transition) of the end cavity, refer to Fig. 9(a), and compared the corresponding wake-loss factors. Although shallow tapering showed a slightly lower value of the wake-loss factor, it increased the characteristic impedance mismatch while running time domain reflection (TDR) simulation. Therefore, we restored the initial tapering strength. The optimization of the characteristic impedance is presented in the following section.

B. Characteristic impedance

We performed time domain reflectometry (TDR) simulations to optimize the characteristic impedance of the kicker along its length. TDR simulation provides information about the magnitude and location of the impedance mismatch, facilitating the fine-tuning of the kicker design to achieve optimal performance. The goal is to reduce this impedance mismatch along its length. To perform TDR simulations, we excite the kicker with a Gaussian pulse. For a Gaussian signal, the rise time, t_{rise} (10%–90%), relates to the upper limit of the frequency band, f_{max} (−20 dB) as [26,27]

$$f_{\mathrm{max}}\,(\mathrm{GHz}) = \frac{0.876}{t_{\mathrm{rise}}\,(\mathrm{ns})}. \tag{8}$$

Although the pulsed power device typically uses a smooth step signal instead of a Gaussian, comparing the TDR obtained by exciting these two signals with the same rise time showed good agreement for a simple coaxial cable-type geometry.

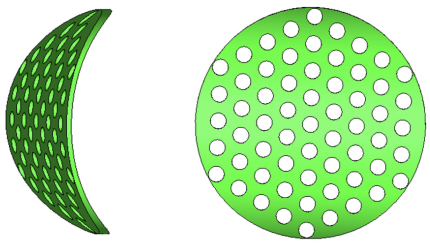

FIG. 11. Updated mesh geometry inside the venting ports; side view (left) and a top view (right).

The rise time of the HSR kicker, see Table I, is $t_{\text{rise}} = 7$ ns, which yields the maximum frequency of $f_{\text{max}} = 0.125$ GHz. However, we choose to excite a signal in the higher frequency range of 0–2 GHz as it offers clearer resolution for the impedance mismatch. In other words, the higher the frequency range, the larger the impedance mismatch will be.

We optimized the characteristic impedance along the length of the HSR kicker by introducing a tapered electrode, adjusting appropriate tapered length of electrode, and tuning the dimension of dielectric (alumina) support and Kovar screw. We discuss these topics in detail in the following subsections.

1. Incorporation of tapered electrode

Our primary strategy to mitigate the unavoidable characteristic impedance mismatch was to incorporate the tapered electrode in the transition region between the feedthrough and electrode. This approach aligns with findings reported in Refs. [6,21,28].

To validate and cross-check the performance of a tapered electrode over nontapered, we compared the TDR plot between them. Figure 12(a) shows the CAD designs of the nontapered (left) and the tapered (right) electrodes, while Fig. 12(b) depicts the TDR comparison between these designs. The comparison demonstrates that the incorporation of tapered electrode lowers the impedance mismatch (magenta curve) significantly in the transition region.

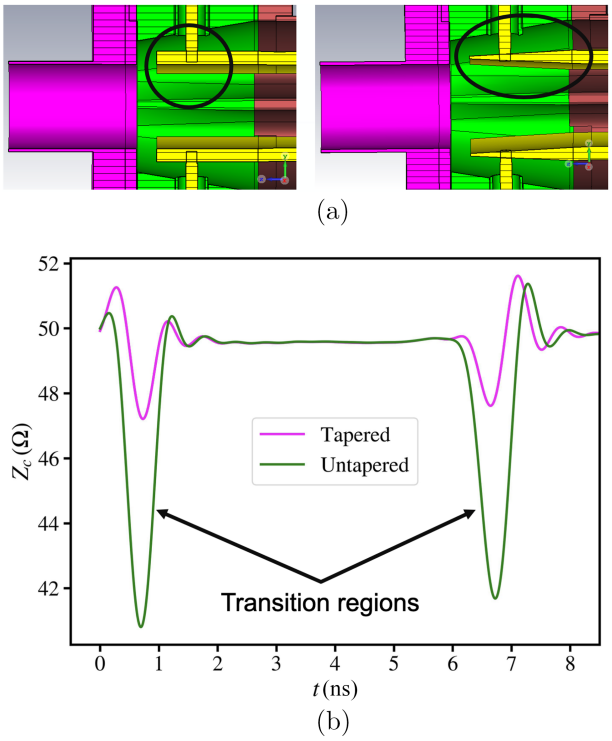

FIG. 12. (a) CAD design showing the nontapered (left) and tapered electrodes (right). (b) TDR plot comparison between the nontapered (green curve) and tapered (magenta curve) electrodes.

2. Optimization of the tapered length and tapering strength

After incorporating the tapered electrode, we further investigated to optimize its tapered length and tapering strength. For this, we prepared four different tapered electrode designs, shown in Fig. 13(a), which we label as V_{13}, V_{14}, V_{15}, and V_{16}, respectively, where V_{13} is the initial design and V_{16} is the optimized design. In the initial design, V_{13}, the tapering strength of the electrode was limited by the larger area of the rf-spring contact, whose dimension was reduced later to enhance tapering strength.

At first, we increased the tapering strength of the electrode in V_{14}, shown in Fig. 13(a), by keeping the same tapered length (~68 mm) as that of V_{13} and compared the TDR plots between them. The comparison, shown in Fig. 13(b), demonstrates that increased tapering strength

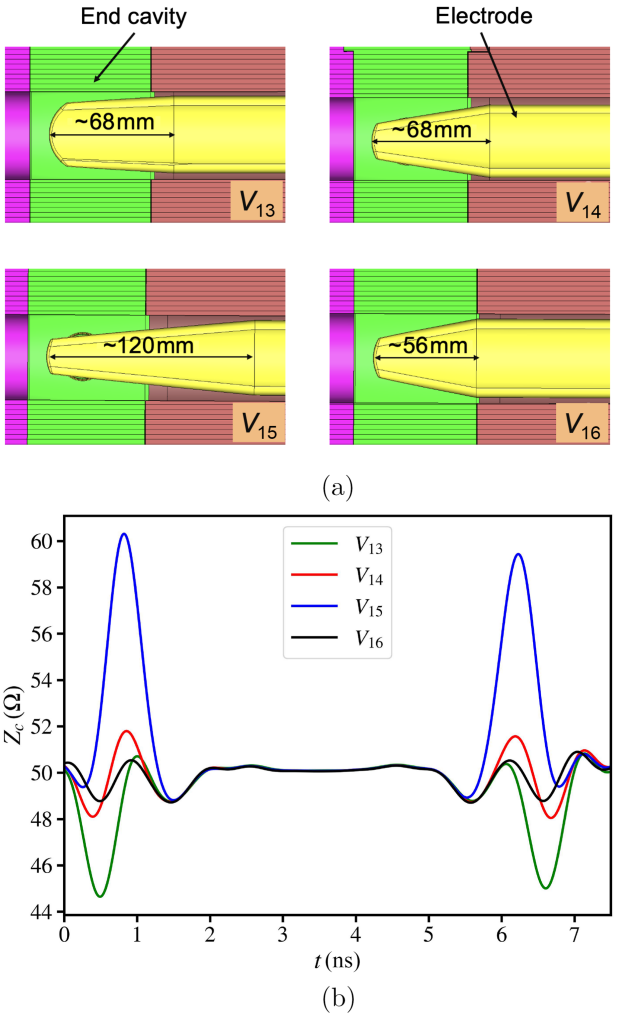

FIG. 13. (a) Four different tapered electrode designs, where V_{13} is the initial tapered design and V_{16} is the optimized design. (b) The TDR comparison corresponds to the designs V_{13} (green curve), V_{14} (red curve), V_{15} (dark blue curve), and V_{16} (black curve).

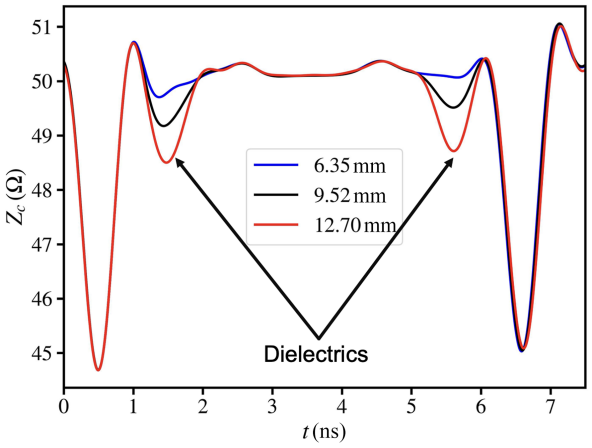

FIG. 14. Characteristic impedance comparison with the diameter of dielectric rod; where the blue, black, and red curves, respectively, represent the diameter of 6.35, 9.52, and 12.70 mm.

lowers the impedance mismatch (red curve) by a factor of ∼2 compared to the initial shallow tapering (green curve).

Subsequently, we increased the tapered length of the electrodes (from ∼68 to ∼120 mm) in V_{15}, to check if we could reduce the impedance mismatch furthermore. However, this adjustment led to significant overshooting (more impedance mismatch), the dark blue curve in Fig. 13(b). Therefore, we explored shortening the tapered length of electrode, even shorter than that of the original value of ∼68 mm. The optimum tapered length for the minimal impedance mismatch was obtained by aligning the tapering (start point) for both the electrode and end-cavity, as depicted in V_{16} of Fig. 13(a). In this case, the tapered length of the electrode is ∼56 mm. The TDR plot corresponding to the optimized tapered length and tapering strength is shown in Fig. 13(b) (black curve).

3. Optimization of the dielectric support dimension

We also tuned the dimension of the dielectric (alumina) supports to reduce the characteristic impedance mismatch. The placement of dielectric support serves the dual purpose of minimizing deflection on the stripline due to its weight and ensuring the alignment of the stripline during feedthrough replacement or adjustment.

Initially, these dielectric supports were excluded from simulations to save computational resources. However, their subsequent inclusion in TDR simulations revealed impedance mismatch. To minimize this mismatch, we reduced the diameter of the dielectric support from its initial value of 12.70 to 9.52 mm. Figure 14 compares the TDR plot for three different dimensions of dielectric support. In fact, a dimension of 6.35 mm demonstrates the best performance, but this small dimension is impractical from a fabrication perspective. Therefore, we chose the dielectric dimension of 9.52 mm. In addition, we decreased the height of dielectric support (from an initial value of 195 to 33 mm), as its height had no impact on the characteristic impedance.

4. Optimization of the Kovar pin

The final component introducing the characteristic impedance mismatch is the height of the Kovar pin (or screw) holding the alumina dielectric. In our earlier simulations, we treated the Kovar metal as alumina as shown in Fig. 15(a) (left) assuming that this pin does not introduce any impedance mismatch being completely inside the alumina. However, modeling the Kovar pin as a metal, shown in Fig. 15(a) (middle), we found that the height of the Kovar pin perturbs the boundary condition and introduces a large impedance mismatch, the green curve in Fig. 15(b).

To minimize this impedance mismatch, we reduced the Kovar pin height significantly from its initial value of 14.2 to 1.3 mm with design modification. The vendor has confirmed the fabrication of this smaller pin design is practical and it can hold the dielectric support effectively. Figure 15(a) shows the CAD models of the Kovar screw's initial design (middle), and optimized design (right), while Fig. 15(b) depicts the TDR comparison between them. The comparison shows that the

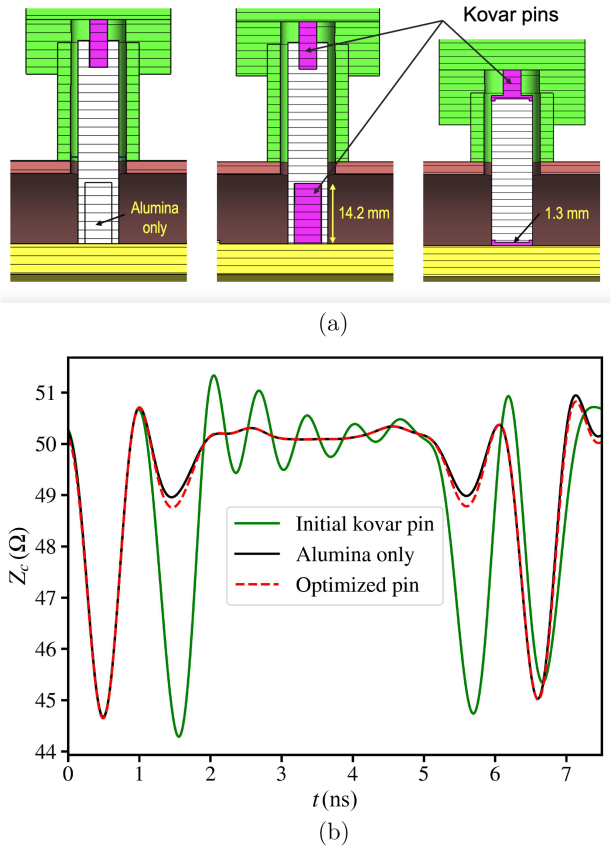

FIG. 15. (a) CAD models showing the different Kovar pin designs: the lower Kovar pin treated as dielectric (left), initial pin design (middle), and the optimized design (right). (b) TDR plot comparison corresponds to these three designs.

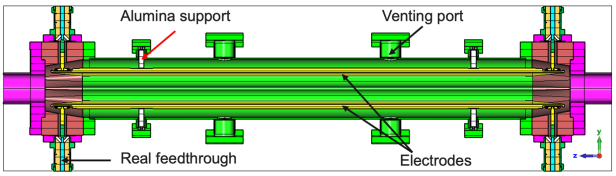

(a)

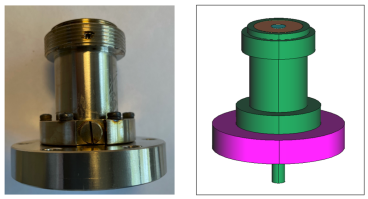

(b)

FIG. 16. (a) Latest design of the kicker geometry with real feedthrough and internal components and (b) photograph of an FID feedthrough (left) and its corresponding reconstructed model based on the FID design (right).

optimized pin reduces the previously observed impedance mismatch significantly (red-dash curve).

The updated geometry of the the kicker, after performing all the optimization discussed in this section, is shown in Fig. 16(a). In this design, we replaced the initial ideal coaxial feedthroughs with real feedthroughs, shown in Fig. 16(b) (right), based on the commercial FID GmbH [29] design [Fig. 16(b), left. Moreover, we recently procured some FID feedthroughs and modified them to enhance their radiation resistance by replacing the air-side dielectric material from polytetrafluoroethylene with high molecular weight polyethylene material.

VI. HEATING AND THERMAL ANALYSIS

We also performed the beam-induced resistive wall (RW) heating and thermal analysis of the HSR kicker. The detailed procedure for this analysis and results for some EIC vacuum chamber components can be found in [30–32]. In summary, we calculate RW loss using CST and feed the loss into another code ANSYS to find the thermal distribution.

We evaluated the RW loss on each component of the kicker, listed in Table IV, using the CST wakefield solver

TABLE IV. Resistive losses on the HSR injection kicker.

Components	Loss (W)
Housing with two-inner flanges	0.78
Two electrodes	0.58
Four-feedthroughs outer cylinder (nickel)	0.68
Four-feedthroughs inner pin (nickel)	0.95
Two end-cavities holding feedthrough	0.19
Four Kovar pins and screws	0.25
Two outer flanges with beam pipe	0.19
Others (venting ports and wire mesh)	0.07
Total	3.69

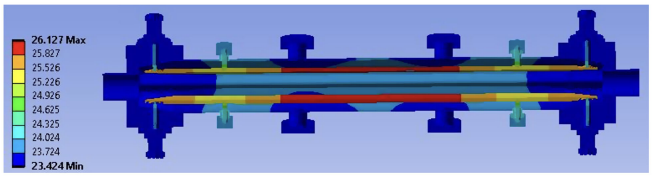

FIG. 17. Thermal analysis for the latest kicker geometry.

for the beam parameters mentioned in Table III. These parameters provide the worst case requirements for beam-induced RW heating. Then, to determine the thermal distribution, we input the RW losses from Table IV into ANSYS, assuming a free convective air on the outside of the kicker housing. The resulting thermal distribution is shown in Fig. 17, which depicts the maximum temperature of 26.13 °C with assuming the room temperature of 22 °C. Hence, active water cooling is not required for this kicker.

For the RW loss calculation, we used 25 μm copper-plated stainless steel material unless otherwise specified. Copper plating reduces the beam-induced RW loss as well as beam coupling impedance. In practice, we put a thin layer (∼nm) of amorphous carbon (aC) on top of the copper coating to reduce secondary electron yield. The effect of the nanometer thick aC-coating in the RW loss was found to be negligible in the simulation.

VII. ELECTRIC FIELD CALCULATION

Finally, we simulated the electric fields for this HSR kicker by exciting a high voltage pulse (16 kV) to ensure the maximum electric field is well below the electric

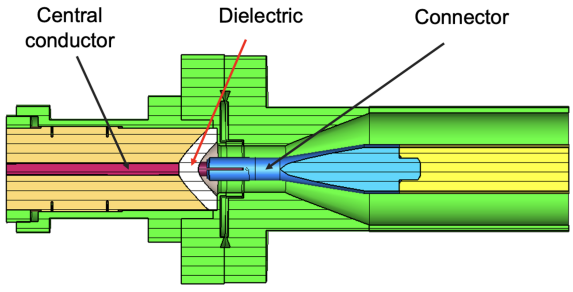

(a)

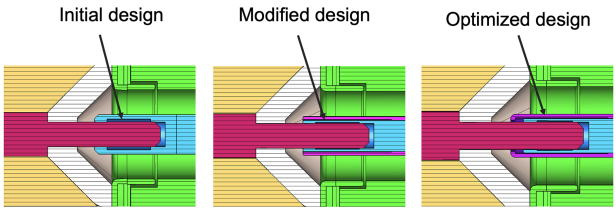

(b)

FIG. 18. (a) Cut view of the initial feedthrough connector showing the longitudinal slot. (b) Three different connector designs: initial (left), modified (middle), and optimized (right).

TABLE V. Maximum electric field calculation due to 16 kV input voltage.

Connector design	Maximum *E*-field (MV/m)
Initial	27.6
Modified	15.6
Optimized	10.8

breakdown or arcing limit. In addition, the power supply will be more reliable for the low fields. To simulate the electric field, we excited a smooth step signal having a rise time of 5 ns (compared to 7 ns in the design) and a flattop of 25 ns via the downstream feedthrough. The initial simulation showed that the maximum electric field occurred in the connecting region of the feedthrough's central conductor. To save computational resources, we focused solely on simulating and optimizing this specific region.

The initial connector design, shown in Fig. 18(a), featured a small longitudinal slit near the dielectric material to insert the center conductor into the feedthrough connector and to ensure a good electrical contact. However, this resulted in a very high value of electric field strength, as shown in Table V, due to sharp edges around the slit. To lower this maximum field, we modified this design by adding a covering sleeve around the connector (magenta colored geometry in Fig. 18(b), middle). The modified design reduced the maximum electric field by a factor of ∼2. Finally, we optimized the connector design with added lips in the covering sleeve and shortening the initial connector length, shown in Fig. 18(b), right. This optimized design reduced the maximum electric field by a factor of ∼3 compared to the initial design.

We listed the maximum electric field value for these three different designs in Table V. Figure 19 shows the contour plot for the maximum electric field for the optimized design. The APS-U kicker has been reported to have a maximum electric field of 16 MV/m [21] for an excitation voltage of 15 kV. In our case, the maximum electric field is obtained as 10.8 MV/m for 16 kV, indicating a more robust design. We also ran simulation for 25 kV pulse voltage for which the maximum field is obtained as 16.8 MV/m. This confirms that operating this kicker up to 25 kV is also acceptable.

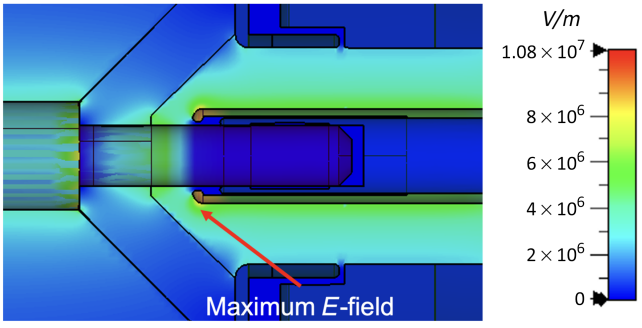

FIG. 19. Maximum electric field in the feedthrough connector due to an input voltage of 16 kV.

VIII. SUMMARY AND FUTURE WORK

In this paper, we reviewed the EIC HSR stripline injection kicker, providing a comprehensive report on its design and optimization. Our design incorporates a novel impedance tuning capability, a critical feature for matching the characteristic impedance of the feedthroughs with the connecting coaxial cable. Our optimization efforts focused on minimizing beam coupling and matching the characteristic impedance. In addition, we presented a beam-induced heating and thermal analysis, which revealed that active water cooling is not required. Finally, we conducted electric field simulations to ensure that the maximum electric field remains below the breakdown threshold, thereby increasing power supply reliability.

A prototype kicker has been successfully fabricated. We are currently conducting leak checks and dc high-voltage tests to validate the optimal performance of the reconstructed feedthrough designs. Our next steps involve rigorous bench testing and cross-checking simulation results for both the kicker and feedthroughs, which are essential for confirming the performance and functionality of our designed components.

ACKNOWLEDGMENTS

The authors are thankful to S. DeSantis of LBNL and K. Tian of SLAC for providing invaluable suggestions and feedback on this kicker design. We also thank K. Hughes, Z. Conway, and A. Zhang for their input on pulsed power throughout this work. Special thanks are extended to Q. Wu, for helping us to optimize feedthrough connector, and S. Peggs for proofreading this article. Furthermore, the authors acknowledge the U.S. Department of Energy, Office of Science, under Contract No. DE-SC0012704, for funding this research.

[1] Electron-Ion Collider, https://www.bnl.gov/eic/.
[2] C. Montag *et al.*, Design status of the Electron-Ion Collider, in *Proceedings of the 14th International Particle Accelerator Conference, IPAC-2023, Venice, Italy* (JACoW, Geneva, Switzerland, 2023).
[3] C. Montag *et al.*, The EIC accelerator: Design highlights and project status, in *Proceedings of the 15th International Particle Accelerator Conference, IPAC-2024, Nashville, TN* (JACoW, Geneva, Switzerland, 2024), pp. 214–217.
[4] All Eyes on EIC at IPAC'24 and in Rome as World Partners Gather, https://www.bnl.gov/newsroom/news.php?a=222000.
[5] M. Sangroula, C. Liaw, C. Liu, N. Tsoupas, S. Verdú-Andrés, B. Xio, and W. Zhang, Optimization of the hadron ring stripline injection kicker for the EIC, in *Proceedings of*

the 12th International Particle Accelerator Conference, IPAC-2021, Campinas, SP, Brazil (JACoW, Geneva, Switzerland, 2021), 10.18429/JACoW-IPAC2021-WEPAB193, https://epaper.kek.jp/ipac2021/papers/wepab193.pdf.

[6] S. De Santis *et al.*, Injection/extraction kicker for the ALS-U project, in *Proceedings of the 5th International Particle Accelerator Conference, IPAC-2014, Dresden, Germany* (JACoW, Geneva, Switzerland, 2014), pp. 1977–1979.

[7] A. W. Chao, H. K. Mess *et al.*, *Handbook of Accelerator Physics and Engineering* (World Scientific, Singapore, 2013).

[8] T. Naito, S. Araki, H. Hayano, K. Kubo, S. Kuroda, N. Terunuma, T. Okugi, and J. Urakawa, Multibunch beam extraction using the strip-line kicker at the KEK accelerator test facility, Phys. Rev. ST Accel. Beams **14**, 051002 (2011).

[9] G. Lambertson, Dynamic devices–pickups and kickers, AIP Conf. Proc. **153**, 1413 (1987).

[10] B. I. Grishanov, F. V. Podgorny, J. Ruemmler, and V. D. Shiltsev, Very fast kicker with high repetition rate for accelerator applications, Nucl. Instrum. Methods Phys. Res., Sect. A **396**, 28 (1997).

[11] S. Peggs and T. Satogata, *Introduction to Accelerator Dynamics* (Cambridge University Press, Cambridge, England, 2017).

[12] F. Willeke *et al.*, Electron-ion collider conceptual design report (2021), https://www.bnl.gov/ec/files/eic_cdr_final.pdf.

[13] C. Belver-Aguilar, A. Faus-Golfe, F. Toral, and M. J. Barnes, Stripline design for the extraction kicker of compact linear collider damping rings, Phys. Rev. ST Accel. Beams **17**, 071003 (2014).

[14] D. M. Pozar, *Microwave Engineering* (John Wiley & Sons, New York, 2011).

[15] R. B. Marks and D. F. Williams, Characteristic impedance determination using propagation constant measurement, IEEE Microwave Guided Wave Lett. **1**, 141 (1991).

[16] A. W. Chao, *Physics of Collective Beam Instabilities in High Energy Accelerators*, Wiley Series in Beam Physics and Accelerator Technology (Wiley-VCH, New York, 1993), https://repository.gsi.de/record/68218.

[17] B. W. Zotter and S. A. Kheifets, *Impedances and Wakes in High-Energy Particle Accelerators* (World Scientific, Singapore, 1998).

[18] M. P. Sangroula, R. R. Lindberg, R. M. Lill, and R. Zabel, Measuring vacuum component impedance for the argonne advanced photon source upgrade, Phys. Rev. Accel. Beams **23**, 082803 (2020).

[19] Opera 2D, Version 2019, https://www.3ds.com/products-services/simulia/products/opera/.

[20] CST Studio Suite, https://www.3ds.com/products-services/simulia/products/cst-studio-suite/solvers/.

[21] X. Sun and C. Yao, Simulation Studies of a Prototype Stripline Kicker for the APS-MBA Upgrade, in *Proceedings of the North American Particle Accelerator Conference, NAPAC-2016, Chicago, IL* (JACoW, Geneva, Switzerland, 2016), https://accelconf.web.cern.ch/napac2016/papers/wepob16.pdf.

[22] K. Tian, J. Langton, N. Parry, J. Safranek, J. J. Sebek *et al.*, Design of a Multi-Bunch Feedback Kicker in SPEAR3, in *Proceedings of the 12th International Particle Accelerator Conference, IPAC-2021, Campinas, SP, Brazil* (JACoW, Geneva, Switzerland, 2021), pp. 327–330.

[23] M. Sangroula, C. Liaw, C. Liu, J. Sandberg, N. Tsoupas, B. Xiao, and X. Sun, Design update on the HSR injection kicker for the EIC, in *Proceedings of the 13th International Particle Accelerator Conference, IPAC-2022, Bangkok, Thailand* (JACoW, Geneva, Switzerland, 2022).

[24] Ansys, https://www.ansys.com/.

[25] N. Wang, S. K. Tian, L. Wang, H. Shi, S. Yue, G. W. Wang, and J. H. Chen, Impedance optimization and measurements of the injection stripline kicker, Phys. Rev. Accel. Beams **24**, 034401 (2021).

[26] Time Domain Reflectometry, https://space.mit.edu/RADIO/CST_online/mergedProjects/3D/common_preloadedmacro/common_preloadedmacro_1d_tdr.htm.

[27] Impedance Simulation of Differential Transmission Lines Considering ESD Protection Diode Components, https://blog.3ds.com/brands/simulia/impedance-simulation-differential-transmission-lines/.

[28] H. Shi, J. H. Chen, L. Wang, N. Wang, L. H. Huo, P. Liu, G. W. Wang, and X. L. Shi, The design and test of a stripline kicker for HEPS, in *Proceedings of the ICFA Advanced Beam Dynamics Workshop, FLS-2018, Shanghai, China* (JACoW, Geneva, Switzerland, 2018), pp. 117–119.

[29] FID GmbH, https://fidtech.com/.

[30] M. Sangroula, J. Bellon, A. Blednykh, D. Gassner, C. Hetzel, C. Liaw, C. Liu, P. Thieberger, and S. Verdu-Andres, Localized beam induced heating analysis for the EIC vacuum chamber components, in *Proceedings of the 5th North American Particle Accelerator Conference, NAPAC 2022, Albuquerque, NM* (JACoW, Geneva, Switzerland, 2022), https://accelconf.web.cern.ch/napac2022/papers/wepa85.pdf.

[31] M. Sangroula, J. Bellon, M. Blaskiewicz, A. Blednykh, P. Braunius, B. Gallagher, D. Gassner, K. Hamdi, C. Hetzel, D. Holmes *et al.*, Beam induced heating analysis update for the EIC vacuum chamber components, Brookhaven National Laboratory (BNL), Upton, NY, Technical Report No. BNL-224903-2023-TECH, 2023, 10.2172/2203271.

[32] M. Sangroula *et al.*, Update on the beam-induced heating and thermal analysis for the EIC vacuum chamber components, in *Proceedings of the International Particle Accelerator Conference, IPAC-2024, Nashville, TN* (JACoW, Geneva, Switzerland, 2024).